

# An Eulerian Data Assimilation Method for Two-Layer Quasi-Geostrophic Model in Physical Domain

Hyeonggeun Yun<sup>1</sup> and Quanling Deng<sup>2,3</sup>

<sup>1</sup>School of Computing, Australian National University, Canberra, ACT 2601, Australia (Geun.Yun@anu.edu.au)

<sup>2</sup>Yau Mathematical Sciences Center, Tsinghua University, Beijing, 100084, China (qldeng@tsinghua.edu.cn)

<sup>3</sup>School of Computing, Australian National University, Canberra, ACT 2601, Australia (Quanling.Deng@anu.edu.au)

November 6, 2025

## Abstract

Data assimilation (DA) integrates observational data with numerical models to improve the prediction of complex physical systems. However, traditional DA methods often struggle with nonlinear dynamics and multi-scale variability, particularly when implemented directly in the physical domain. To address these challenges, this work develops an Eulerian Data Assimilation (EuDA) method with the Conditional Gaussian Nonlinear System (CGNS). The proposed approach enables the treatment of systems with non-periodic boundaries and provides a more intuitive representation of localized and time-dependent phenomena. The work considers a simplified physical domain inspired by sea-ice floe trajectories and ocean eddy recovery in the Arctic regions, where the dynamics are modeled by a two-layer quasi-geostrophic (QG) system. The QG equations are numerically solved using forward-Euler time stepping and centered finite-difference schemes. CGNS provides a nonlinear filter as it offers an analytical and continuous formulation for filtering a nonlinear system. Model performance is assessed using normalized root mean square error (RMSE) and pattern correlation (Corr) of the posterior mean. The results show that both metrics improve monotonically with refining timesteps, while RMSE converges to approximately 0.1, which is the noise strength, and Corr increases from 0.64 to 0.92 as the grid resolution becomes finer. Lastly, a coupled scenario with sea-ice particles advected by the two-layer QG flow under a linear drag force is examined, demonstrating the flexibility of the EuDA-CGNS framework in capturing coupled ice-ocean interactions. These findings demonstrate the effectiveness of exploiting the two-layer QG model in the physical domain to capture multiscale flow features.

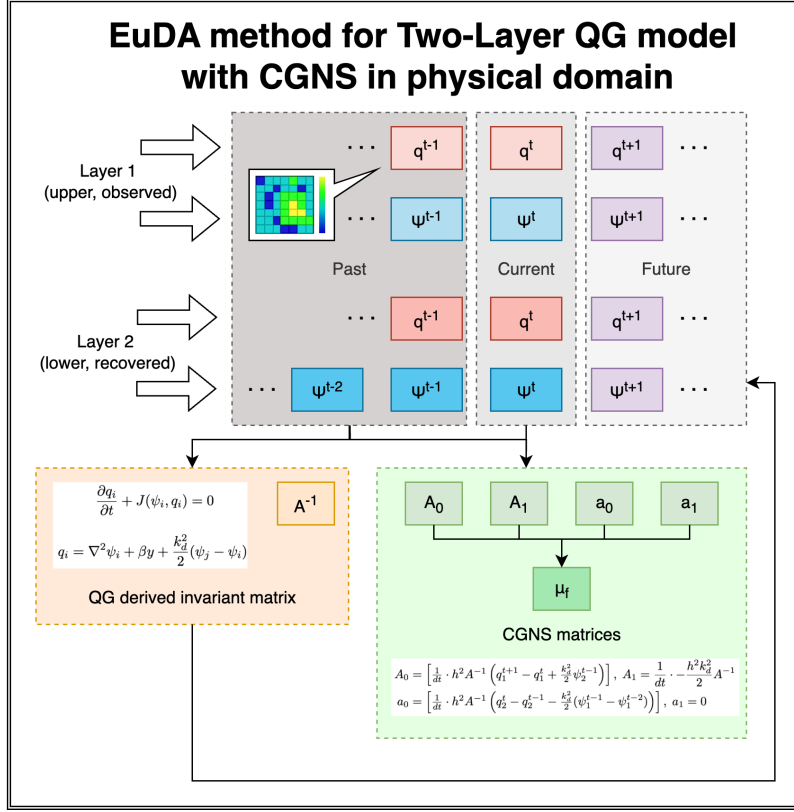
**Keywords:** Data assimilation, quasi-geostrophic model, conditional nonlinear Gaussian system

# 1 Introduction

Data assimilation (DA) has become an essential tool for improving predictions of complex physical systems, especially in fields like meteorology, oceanography, and climate science, where observational data are sparse or noisy with high uncertainties [1, 16]. The purpose of DA is to merge observational data with numerical model predictions to achieve an optimal estimate of the system’s state [16]. By assimilating real-time observations into predictive models, DA can reduce state estimation errors and enhance the overall prediction.

Traditional DA methods, however, face limitations when applied to systems characterized by multi-scale dynamics and significant nonlinearity. Lagrangian DA, for example, is well-suited to capturing small-scale structures through particle trajectories but is computationally demanding due to high dimensionality and nonlinearity in the Lagrangian observations [12]. On the other hand, Eulerian Data Assimilation (EuDA) provides computational efficiency in representing large-scale flow fields on fixed grids, yet often lacks the resolution needed for smaller-scale features [17]. These challenges are exacerbated in environments with both large-scale and fine-scale structures, such as ocean eddies or atmospheric fronts, where accurate tracking of particle movements is essential for high-fidelity modeling [27]. Out of these two DA methodologies, this work develops an EuDA method formulated directly in a simplified physical domain to recover the physical attributes, inspired by the real application of modeling sea ice floe dynamics in polar regions. This framework enables the model to capture localized, time-dependent phenomena more intuitively compared to other commonly used methods in spectral or Fourier space.

We focus on a two-layer quasi-geostrophic (QG) system for providing a simplified yet physically grounded representation of large-scale geophysical flows. The QG model captures essential barotropic and baroclinic interactions, and remains a cornerstone in studies of mid-latitude atmospheric and oceanic dynamics [2, 27]. In this context, the Eulerian framework is enhanced through the Conditional Gaussian Nonlinear System (CGNS), which allows continuous and analytically tractable filtering for nonlinear dynamical systems. This is achieved through exploitation of the conditional Gaussian structure, which provides closed-form expressions for conditional mean and covariance, enabling efficient and stable assimilation without ensemble sampling [5].



The main objective of this study is to evaluate the effectiveness of applying the EuDA framework based on CGNS to the two-layer QG model (see Figure 1) in the physical domain. The performance of the assimilated posterior mean is assessed using root mean square error (RMSE) and pattern correlation (Corr), which collectively measure estimate accuracy and spatial coherence. The results demonstrate that the EuDA approach can recover physically consistent fields while maintaining computational efficiency.

The rest of the paper is organized as follows. Section 2 presents the formulation of the two-layer QG model and describes the numerical schemes for both spatial and temporal discretizations. Section 3 details the proposed EuDA method using CGNS. Section 4 discusses numerical experiments, including simulation results and their evaluation. Finally, Section 5 concludes the paper with remarks and potential future extensions of this work.

## 2 Problem statement and numerical schemes

### 2.1 Two-layer quasi-geostrophic (QG) model

As the aim of the research focuses on the data assimilation framework in the physical domain for a specific landscape like the Arctic, careful consideration is required in adopting the ocean or atmospheric model. The QG model was deemed to be suitable with the following assumptions. The model is underpinned by a small Rossby number ( $R_o \ll 1$ ) that makes the flow nearly geostrophic, which implies significantly smaller inertia forces than Coriolis forces [32, 10]. The Rossby number is given by  $R_o = \frac{U}{fL}$ , where  $U$  is a typical horizontal velocity,  $L$  is the horizontal length scale, and  $f$  is the Coriolis parameter. Such a discrepancy suits a condition with predominantly horizontal flow. Another underlying assumption is the assertion of a hydrostatic balance in vertical motion [32, 10]. This means the vertical pressure gradient is balanced by the gravitational force, effectively allowing the model to ignore vertical accelerations. This is captured by the equation  $\frac{\partial p}{\partial z} = -\rho g$ , where  $p$  is the pressure,  $z$  is the vertical coordinate,  $\rho$  is the fluid density and  $g$  is the acceleration due to gravity. Furthermore, the flow is assumed to be incompressible in baroclinic models, which means the density does not change significantly with time or space in the horizontal directions [32, 10]. This assumption makes the use of a constant density possible. Altogether, it should be clear that the assumptions resemble large-scale, slow-moving flows in the ocean and atmosphere, such as those found in the polar regions.

The main advantage of the QG model in the given context is its simplicity to work for two layers. This two-layer QG can recover the important physical attributes at one depth, such as streamfunction ( $\psi$ ) and potential vorticity ( $q$ ), by observing those of other depths. In simplified form, the two-layer QG governing equations are [32, Sect. 5]:

$$\frac{\partial q_i}{\partial t} + J(\psi_i, q_i) = 0, \quad (1)$$

$$\nabla^2 \psi_i + \beta y + \frac{k_d^2}{2}(\psi_j - \psi_i) = q_i, \quad (2)$$

where  $i = \{1, 2\}$  denotes the level index,  $j = 3 - i$  and the Jacobian is  $J(\psi_i, q_i) = \frac{\partial \psi}{\partial x} \frac{\partial q}{\partial y} - \frac{\partial \psi}{\partial y} \frac{\partial q}{\partial x}$ . For well-posedness, the two-layer QG model is subject to initial and boundary conditions, which will be specified later for the simulations. For the sake of simplicity, the model is assumed to have no external force on the surface and the depths of layers are even. Hence, the assumptions result in 0 for the RHS of Equation (1) and  $\frac{k_d^2}{2}$  for Equation (2), respectively. Along with the assumptions, Table 1 illustrates the scale of the model, by providing the typical order of magnitude of relevant parameters. These are nondimensionalized and scaled accordingly throughout any computation involving the QG model (see Table 3). The Laplacian discretization constant will further be discussed in Section 2.2.2, as it has been manually derived from the discretization process.

Physical quantities	Symbol	Typical order of magnitude
streamfunction	$\psi$	$10^3 \sim 10^5 m^2 s^{-1}$
Potential vorticity	$q$	$10^{-6} \sim 10^{-5} s^{-1}$
Coriolis parameter	$f_0$	$10^{-4} s^{-1}$
Beta parameter	$\beta$	$10^{-11} t^{-1} s^{-1}$
Rossby radius of deformation	$L_d$	$50 \sim 100 km$
Layer thickness	$H$	$100 \sim 1000 m$
Buoyancy frequency	$N$	$10^{-2} s^{-1}$
Square of the deformation wavenumber	$k_d^2$	$10^{-9} m^{-2}$

Table 1: Parameters for the two-layer QG model with their typical order of magnitude.

Despite a clear existence of coupling between layers from Equation (2), the decoupling of the two layers for the DA setting is relatively simple as  $\psi_j$  only appears once from the perspective of layer  $i$ . Another notable insight is the absence of a time-derivative term for  $\psi_i$ , insinuating its necessity to couple with  $q_i$  to exploit the parameter in a temporal perspective. These relationships provide the dynamical basis for the Eulerian assimilation framework developed in Section 3, where the coupled evolution of  $\psi$  and  $q$  forms the state equations in the CGNS.

For the DA filtering process, one augments each prognostic PV equation with an additive process-noise term that represents unresolved physics and model error; this noise is taken to be Gaussian white noise and typically spatially correlated through a prescribed covariance (see, e.g., [29]). To keep the numerical scheme presentation straightforward, we omit this stochastic term in the model discretization exposition and introduce it later when applying the DA method as part of the overall modeling and discretization errors in the assimilation setup.

## 2.2 Numerical schemes

### 2.2.1 Temporal discretization

Various time-integration schemes have been developed for QG models, including Leapfrog, Runge-Kutta, and semi-implicit formulations [3, 23, 24]. These higher-order approaches often achieve greater accuracy and phase stability for oscillatory flows but introduce additional computational cost and complexity. Given that the primary goal of this study is to establish and evaluate the EuDA framework formulated under the CGNS, the error is dominated by the noise terms; thus, a simple explicit time-stepping scheme is sufficient. Accordingly, we use the first-order explicit forward-Euler step for time discretization of the deterministic two-layer QG equation. When the additive Gaussian white noise is introduced in the data assimilation setting, the natural counterpart is the Euler-Maruyama scheme: it retains the forward-Euler update and augments each step with a mean-zero Gaussian increment where spatial covariance matches the prescribed model-error covariance

and magnitude scales with the square root of the time step. In practice, the noise field at each step is generated by sampling i.i.d. standard normals, mapping them through a square root of the spatial covariance, and scaling by the square root of the time step. For clarity of exposition, we present the core scheme with forward Euler and introduce the Euler-Maruyama augmentation when the DA method is applied.

Let  $T > 0$  be the final time and choose an integer  $N \geq 1$  as the number of time steps. Define the uniform time step  $\Delta t := T/N$  and the grid points  $t^n := n \Delta t, n = 0, 1, \dots, N$ , so that  $0 = t^0 < t^1 < \dots < t^N = T$ . The forward-Euler scheme approximates the temporal derivative of a state variable  $\phi$  (e.g., potential vorticity or streamfunction) of equation  $\frac{d\phi}{dt} = f(\phi, t)$  as

$$\phi^{n+1} = \phi^n + \Delta t f(\phi^n, t^n), \quad (3)$$

where  $f(\phi^n)$  denotes the governing tendency term evaluated at the current time level. Despite being first-order accurate in time, the method is straightforward to implement and ensures a transparent relationship between consecutive states  $\phi^n$  and  $\phi^{n+1}$ , which aligns naturally with the conditional mean and covariance updates in the CGNS formulation. The simplicity of the explicit formulation also facilitates direct control of numerical stability and error propagation, which is advantageous for diagnosing the physical consistency of the assimilation process [21, 15]. To maintain numerical stability, the time step  $\Delta t$  was chosen to satisfy the Courant-Friedrichs-Lewy (CFL) criterion [9]. In this study,  $\Delta t = 10^{-4}$  was found to provide a balance between accuracy and computational efficiency for the QG model.

The forward-Euler method advances the prognostic variable  $q_i$  of each layer as

$$q_i^{n+1} = q_i^n - \Delta t J(\psi_i^n, q_i^n), \quad (4)$$

where  $J(\psi_i, q_i)$  is the Jacobian representing the nonlinear advection of potential vorticity. The resulting updated vorticity field is then inverted to obtain the new streamfunction  $\psi_i^{t+\Delta t}$  via the discretized elliptic relation described in the following subsection. This sequential update forms the backbone of the numerical solver that generates the forecast state for the Eulerian assimilation procedure. In summary, while higher-order schemes could offer enhanced temporal accuracy, the forward-Euler approach was deliberately chosen for simplicity, conceptual transparency, computational tractability, and most importantly, suitability for data assimilation schemes.

### 2.2.2 Spatial discretization

Let the two-layer QG model Equations (1) and (2) be defined on the unit-square domain  $\Omega = [0, 1] \times [0, 1]$ . Consider a uniform grid of size  $N_x \times N_y$  with  $h_x := \frac{1}{N_x}, h_y := \frac{1}{N_y}$ , and grid nodes  $x_i := i h_x (i = 0, \dots, N_x), y_j := j h_y (j = 0, \dots, N_y)$ . For a sufficiently smooth scalar field  $u : \bar{\Omega} \rightarrow \mathbb{R}$ ,

denote its grid values by  $u_{i,j} \approx u(x_i, y_j)$ . Interior indices are  $\mathcal{I} = \{1, \dots, N_x - 1\} \times \{1, \dots, N_y - 1\}$ . With this setting in mind, the governing equations are rewritten as

$$\frac{\partial q_i}{\partial t} + \frac{\partial \psi_i}{\partial x} \frac{\partial q_i}{\partial y} - \frac{\partial \psi_i}{\partial y} \frac{\partial q_i}{\partial x} = 0, \quad (5)$$

$$\nabla^2 \psi_i + \beta y + \frac{k_d^2}{2} (\psi_j - \psi_i) = q_i. \quad (6)$$

They are discretized at each grid cell  $(x_k, y_l)$  for layers  $i, j \in \{1, 2\}$  using the second-order central finite difference method [27]. Firstly, with the forward Euler scheme for the temporal dimension, the Jacobian term in Equation (5) is computed as:

$$q_{k,l}^{n+1} - q_{k,l}^n = \left( \frac{\psi_{k,l+1}^n - \psi_{k,l-1}^n}{2h_y} \frac{q_{k+1,l}^n - q_{k-1,l}^n}{2h_x} - \frac{\psi_{k+1,l}^n - \psi_{k-1,l}^n}{2h_x} \frac{q_{k,l+1}^n - q_{k,l-1}^n}{2h_y} \right) \Delta t, \quad (7)$$

where the superscript denotes the time marching. This update is combined with the temporal scheme from Section 2.2 to advance  $q$  explicitly at each time step.

The streamfunction  $\psi_i$  is obtained by numerically inverting the elliptic relation Equation (6). Rearranging gives  $\nabla^2 \psi_i - \frac{k_d^2}{2} \psi_i = q_i - \beta y - \frac{k_d^2}{2} \psi_j$ . Consider a uniform grid case with  $h_x = h_y = h$ . We apply the same finite-difference scheme to the Laplacian to obtain

$$\frac{\psi_{i_{k+1,l}} + \psi_{i_{k-1,l}} + \psi_{i_{k,l+1}} + \psi_{i_{k,l-1}} - 4\psi_{i_{k,l}}}{h^2} - \frac{k_d^2}{2} \psi_{i_{k,l}} = \hat{F}_{k,l}, \quad (8)$$

with  $\hat{F}_{k,l} = q_{i_{k,l}} - \beta y_l - \frac{k_d^2}{2} \psi_{j_{k,l}}$  being the right-hand side. This can be compactly written in matrix form as

$$A\psi = F. \quad (9)$$

For the entries near boundaries, we apply the doubly periodic boundary conditions in both  $x$  and  $y$  directions:  $\psi_i(0, y, t) = \psi_i(L_x, y, t)$ ,  $\psi_i(x, 0, t) = \psi_i(x, L_y, t)$ .

We remark that alternative spatial discretizations, such as finite element [14, 13] or isogeometric analysis [8, 11], can be adopted when geometric fidelity or unstructured meshes are required. In this work, we use a standard second-order central finite-difference scheme on a uniform grid to keep the implementation simple and to focus on the data assimilation (DA) workflow. For our objectives, higher-order spatial accuracy is not rate-limiting: the dominant errors arise from the DA process and model uncertainty rather than from spatial truncation. The proposed DA framework remains unchanged if a different consistent spatial discretization is employed.

### 2.2.3 Numerical setup

With the temporal and spatial discretization schemes, the numerical implementation solves for  $\psi_i$  and  $q_i$  on a two-dimensional, uniform grid iteratively as follows. The two governing Equations (5) and (6) are coupled at each time step, where Equation (5) provides the prognostic update for  $q_i$ , and Equation (6) yields the diagnostic inversion for  $\psi_i$ . These operations define the matrices  $A_0, A_1, a_0$ , and  $a_1$  that later appear in the CGNS filtering stage (see Section 3.1).

Analytical integration of these equations is intractable due to the high dimensionality and strong nonlinear coupling between layers [28]. The discretized numerical model, therefore, serves as the benchmark generator for testing the CGNS-based assimilation scheme. In this work, a full simulation involves grids up to  $50 \times 50$  and  $2 \times 10^4$  time steps. Direct analytical evaluation would require symbolic manipulation of large trigonometric expressions and matrix exponentials, which would take several days in MATLAB, whereas the present finite-difference solver completes within approximately 30 minutes on a standard workstation.

All simulation parameters are summarized in Tables 2 and 3.

Name	Symbol	Simulation Parameters
Final time	$T_f$	$0.05 \sim 2s$
Time-step size	$dt$	$10^{-4} s$
Mesh grid setting	$N_x \times N_y$	$\{10 \times 10, 30 \times 30, 50 \times 50\}$
Initial streamfunction 1 (asymmetric sinusoidal)	$\psi_i^{t=0}$	$\psi_1^{t=0}(x, y) = 0.6 \cos(2.3\pi x) \cos(2.8\pi y) - \sin(1.2\pi x) \sin(1.5\pi y)$
Initial streamfunction 2 (symmetric Gaussian)	$\psi_i^{t=0}$	$\psi_2^{t=0}(x, y) = \sin(3.1\pi x) \sin(0.8\pi y) + 0.7 \cos(1.6\pi x) \cos(2.4\pi y)$
Smoothing kernel dimension	$n \times n$	$\psi_1^{t=0}(x, y) = \exp(-32(2(x-1/2)^2 + (y-1/2)^2))$ $\psi_2^{t=0}(x, y) = \exp(-\frac{64}{3}((x-1/2)^2 + 4(y-1/2)^2))$ $5 \times 5$

Table 2: Temporal and spatial parameters of the simulation.

Name	Symbol	Parameter Dimensions
Streamfunction	$\psi$	$10^{-2} \sim 10^{-1}$
Potential vorticity	$q$	$10 \sim 10^2$
Coriolis parameter	$f_0$	$10^{-2}$
Beta parameter	$\beta$	$10^{-1}$
Rossby radius of deformation	$L_d$	$50 \sim 100$
Layer thickness	$H$	$100 \sim 1000$
Buoyancy frequency	$N$	$10^{-4} \sim 10^{-3}$
Square of deformation wavenumber	$k_d^2$	$10$

Table 3: Nondimensionalized parameters used for the two-layer QG model.

The spatial unit square domain  $[0, 1] \times [0, 1]$  is discretized into  $N_x \times N_y$  uniform cells. The time increment  $\Delta t = 10^{-4}$  satisfies the CFL condition for stability. Two initial conditions are tested: (1) an asymmetric sinusoidal pattern and (2) a symmetric Gaussian field. The former generates complex, chaotic advection patterns representative of realistic mesoscale eddies, and thus is used

as a benchmark experiment for the proposed method, while the latter serves as a sanity check for model stability.

For the well-posedness of the two-layer QG model, we impose homogeneous boundary conditions on the streamfunctions. At each time step,  $q^{n+1}$  is computed explicitly from  $q^n$  and  $\psi^n$  using Equation (7), and  $\psi^{n+1}$  is recovered by solving the linear system in Equation (9). The overall numerical workflow is summarized in Algorithm 1. Because matrix  $A$  remains constant, its decomposition is performed once before the time-marching loop, allowing the update of  $\psi$  and  $q$  at each iteration to proceed efficiently.

---

**Algorithm 1** Two-layer QG numerical solver

---

**Require:** {all the parameters in Tables 2 and 3}  
**initialize** temporal and spatial discretization parameters and  
**initialize** and precompute the invariant matrix  $A$  before time marching  
**initialize**  $\psi^1$  and  $q^1$  from the initial  $\psi$   
**for**  $j \leftarrow 1$  **to**  $N_t$  **do**  
    **compute**  $q^{j+1}$  by solving Equation (1) with Equation (7)  
    **compute**  $\psi^{j+1}$  by solving Equation (2) with Equation (9)  
**end for**  
**return**  $\psi^{1:N_t}$  and  $q^{1:N_t}$

---

### 3 Eulerian data assimilation (EuDA)

#### 3.1 Conditional Gaussian nonlinear system (CGNS)

The CGNS offers a powerful framework to model complex dynamical systems that exhibit both nonlinear and non-Gaussian characteristics [22, 6, 5, 4]. In these systems, while the overall dynamics may be highly nonlinear, the conditional distributions of specific variables retain a Gaussian structure [4, 5]. This property is especially beneficial for data assimilation as it enables closed-form solutions for conditional mean and covariance, streamlining the analysis and computational tasks associated with high-dimensional, nonlinear systems [20, 33].

The framework typically uses two state variables,  $X$  (observational) and  $Y$  (estimation). It should be noted that each state variable is defined in multi-dimension (i.e.  $X \in \mathbb{C}^{n_1}$  and  $Y \in \mathbb{C}^{n_2}$ ), as exemplified in Section 3.2. With such state variables, the general form of the CGNS is expressed as:

$$dX = [A_0(X, t) + A_1(X, t)Y] dt + B_1(X, t)dW_1(t), \quad (10)$$

$$dY = [a_0(X, t) + a_1(X, t)Y] dt + b_1(X, t)dW_2(t), \quad (11)$$

where  $A_0, A_1, a_0, a_1$  denote the system matrices that may vary with both  $X$  and time  $t$ , while noise-strength matrices  $B_1$  and  $b_1$  incorporate stochasticity through independent Wiener processes  $W_1$  and  $W_2$  [4, 25]. One property of the system is its continuity in observing and recovering, unlike traditional data assimilation frameworks, such as the Kalman filter [18, Sect. 21] and Ensemble Kalman filter [30]. This requires more observational data but leads to a smoother propagation of uncertainties over time.

Another key advantage of the CGNS lies in the conditional Gaussian structure, which allows  $Y$ , conditioned on  $X$ , to follow a linear Gaussian process. This relationship simplifies the computation of conditional mean ( $\mu_f$ ) and conditional covariance ( $R_f$ ), which can be derived using the following closed-form expression [20, 4]:

$$d\mu_f = (a_0 + a_1\mu_f) dt + (R_f A_1^*)(B_1 B_1^*)^{-1} (dX - (A_0 + A_1\mu_f)dt), \quad (12)$$

$$dR_f = [a_1 R_f + R_f a_1^* + b_1 b_1^* - (R_f A_1^*)(B_1 B_1^*)^{-1} (A_1 R_f)]dt, \quad (13)$$

where  $.$  is the complex conjugate transpose. This is to be treated as the transpose ( $.^n$ ) in the paper, as all values are real numbers. These equations form the basis for optimal filtering within CGNS and enable efficient, scalable computations in high-dimensional systems, such as oceanographic and atmospheric models.

Nevertheless, the most difficult and critical part when implementing the framework involves the derivation of system matrices, especially  $A_1$  and  $A_0$ , which are responsible for the coupling between observed and predicted variables, especially as Equation (6) does not involve time-dependency explicitly. The construction of matrices and their impact on the stability will be the main discussion of Sections 3.2 and 3.3.

## 3.2 EuDA for recovery of the vorticity

As a step towards more realistic and complicated cases, CGNS is first utilized to recover vorticity  $q$  given its streamfunction  $\psi$  for both layers. To recover the vorticity, we consider the observational state and recovery state as below.

$$X = \begin{bmatrix} \psi_1 \\ \psi_2 \end{bmatrix}, Y = \begin{bmatrix} q_1 \\ q_2 \end{bmatrix}. \quad (14)$$

With this setting and the discretization in mind, we need to write the modeling system Equations (1) and (2) in the form of Equations (10) and (11). Since Equation (2) has no time-derivative term, we substitute Equation (2) into Equation (1) to obtain

$$\frac{\partial(\nabla^2 \psi_i + \beta y + \frac{k_d^2}{2}(\psi_j - \psi_i))}{\partial t} + J(\psi_i, q_i) = 0, \quad (15)$$

which reduces to

$$\frac{\partial \psi_j}{\partial t} = \frac{1}{k_d^2} (\partial_t (k_d^2 \psi_i - 2\nabla^2 \psi_i) - 2J(\psi_i, q_i)). \quad (16)$$

Herein, we used  $\frac{\partial(\beta y)}{\partial t} = 0$ . Rewriting Equation (1) as  $\frac{\partial q_i}{\partial t} = -J(\psi_i, q_i)$  and combining it with the above equation leads to the CGNS form. Applying the numerical schemes in Section 2.2 to the following differentials leads to the corresponding vectors and matrices in CGNS:

$$A_0 \sim \frac{1}{k_d^2} \begin{bmatrix} \partial_t (k_d^2 \psi_2 - 2\nabla^2 \psi_2) \\ \partial_t (k_d^2 \psi_1 - 2\nabla^2 \psi_1) \end{bmatrix}, \quad A_1 Y \sim \frac{2}{k_d^2} \begin{bmatrix} -J(\psi_2, q_2) \\ -J(\psi_1, q_1) \end{bmatrix}, \quad (17)$$

$$a_0 = \begin{bmatrix} 0 \\ 0 \end{bmatrix}, \quad a_1 Y \sim \begin{bmatrix} -J(\psi_1, q_1) \\ -J(\psi_2, q_2) \end{bmatrix}, \quad (18)$$

where  $\sim$  refers to the correspondence of vectors and matrices generated from the differentials after discretization. We note that  $A_1$  is an anti-diagonal block matrix and  $a_1$  is a diagonal block matrix such that  $A_1 Y$  and  $a_1 Y$  are vectors of the above form. These nonzero matrices guarantee the observability for data assimilation. For controllability, let  $B_1, b_1$  be the nonzero noise terms, and in the numerical experiments, we set noise covariance matrices as diagonal matrices with constant diagonal values  $\sqrt{5}$  for  $B_1$  and 0.1 for  $b_1$ , respectively. This setting assumes larger noise/error in the discretization of  $\psi_i$  for  $X$  as it involves second-order spatial derivatives. Using the Euler-Maruyama method, the Wiener process terms are characterized as  $dW_1, dW_2 = \mathbf{Rand}(0, 1)\sqrt{dt}$  for each entries of the state vectors [19]. With this in mind, Algorithm 2 below outlines the entire data assimilation process.

---

**Algorithm 2** CGNS Recovery of the Vorticity

---

**Require:** {all the parameters in Tables 2 and 3}  
**initialize** parameters, grid settings, and initial and boundary states  
**for**  $j \leftarrow 1$  **to**  $N_{t_0}$  (computing statistics for initial posterior mean and variances) **do**  
    **compute**  $q^{j+1}$  via Equation (1) with Equation (7)  
    **compute**  $\psi^{j+1}$  via Equation (2) with Equation (9)  
    **update**  $\Sigma\psi$  and  $\Sigma q$  for  $R_f$   
**end for**  
**initialize**  $R_f$  from  $\psi^{1:N_{t_0}}, \Sigma\psi, q^{1:N_{t_0}},$  and  $\Sigma q$   
**generate** true trajectories and observational data  
**for**  $j \leftarrow N_{t_0}$  **to**  $N_t$  **do**  
    **form**  $A_0, A_1, a_0, a_1$  using numerical discretization of Equations (17) and (18)  
    **compute** prior using Euler-Maruyama method for Equations (10) and (11)  
    **compute** posterior mean via Equation (12) and covariance via Equation (13)  
**end for**  
**return** posterior means and covariances and evaluate skill scores

---

### 3.3 EuDA for recovery of the second layer

In the above subsection, we outlined the application of CGNS to recover the vorticity. In this subsection, we consider  $\psi_1$  as the only observation with the goal of recovering the physical quantities of the second layer. We first observe that one may solve for vorticity using Equation (1) or Equation (2) as an auxiliary step in a deterministic way to reduce the dimensions of the state variables in the data assimilation setting (see, for example, [29]).

We consider the setting of state variables as  $X \sim [\psi_1], Y \sim [\psi_2]$ . In light of the matrix form in Equation (9) and using Equation (1), we take the difference of the inverse of Equation (9) at time steps  $t_j$ , and  $t_{j+1}$  to arrive at

$$\begin{aligned} d\psi_1|_{t_{j+1}} &:= \psi_1^{j+1} - \psi_1^j = A^{-1} \left( q_1^{j+1} - q_1^j - \frac{k_d^2}{2} (\psi_2^{j+1} - \psi_2^j) \right), \\ &= -A^{-1} \left( J(\psi_1^j, q_1^j) dt + \frac{k_d^2}{2} (\psi_2^{j+1} - \psi_2^j) \right), \\ &= -A^{-1} \left( J(\psi_1^j, q_1^j) dt + \frac{k_d^2}{2} (\psi_2^j - \psi_2^{j-1}) \right) + \mathcal{O}(dt)^2, \end{aligned} \quad (19)$$

where the Taylor expansion is used for the term  $\mathcal{O}(dt)^2$ . Similarly, we approximate  $\psi_2$  as

$$\begin{aligned} d\psi_2|_{t_{j+1}} &:= \psi_2^{j+1} - \psi_2^j = A^{-1} \left( q_2^{j+1} - q_2^j - \frac{k_d^2}{2} (\psi_1^{j+1} - \psi_1^j) \right), \\ &= A^{-1} \left( q_2^j - q_2^{j-1} - \frac{k_d^2}{2} (\psi_1^j - \psi_1^{j-1}) \right) + \mathcal{O}(dt)^2, \\ &= -A^{-1} \left( J(\psi_2^{j-1}, q_2^{j-1}) dt + \frac{k_d^2}{2} (\psi_1^j - \psi_1^{j-1}) \right) + \mathcal{O}(dt)^2, \end{aligned} \quad (20)$$

where Equation (1) is used for vorticity time-difference at a previous time step to alleviate the strong nonlinearity in  $Y \sim [\psi_2]$  to formulate Equation (11). In other words,  $J(\psi_2^{j-1}, q_2^{j-1})$  is used here as known from previous estimation, thus resembling the  $a_0$  term in Equation (11). If one uses  $J(\psi_2^j, q_2^j)$ , it leads to a nonlinear term of form  $a_1(Y, t)Y$  in Equation (11) since  $q_2$  is written in terms of  $\psi_2$  as in Equation (2). In the case of a term  $a_1(Y, t)Y$  instead of  $a_1(X, t)Y$  in Equation (11), there are no closed-form solutions to the CGNS Equations (10) and (11).

With the above derivation, applying the numerical schemes in Section 2.2 to the following differentials leads to the corresponding vectors and matrices in CGNS:

$$A_0 \sim -A^{-1} \left( J(\psi_1^j, q_1^j) - \frac{k_d^2}{2dt} \psi_2^{j-1} \right), \quad A_1 Y \sim -A^{-1} \frac{k_d^2}{2dt} \psi_2^j, \quad (21)$$

$$a_0 \sim -A^{-1} \left( J(\psi_2^{j-1}, q_2^{j-1}) + \frac{k_d^2}{2dt} (\psi_1^j - \psi_1^{j-1}) \right), \quad a_1 = 0, \quad (22)$$

where  $\sim$  refers to the correspondence of vectors and matrices generated from the differentials after discretization. Herein, we remark that the matrix  $A^{-1}$  does not need to be constructed explicitly. In numerical simulations, it is usually converted to solving linear systems of equations using  $A$  directly. With this in mind, the pseudo-code for the data assimilation of the second-layer information is outlined in Algorithm 3.

---

**Algorithm 3** CGNS Recovery of the Second-Layer

---

**Require:** {all the parameters in Tables 2 and 3}  
**initialize** parameters, grid settings, matrix  $A$ , and initial and boundary states  
**for**  $j \leftarrow 1$  **to**  $N_{t_0}$  (computing statistics for initial posterior mean and variances) **do**  
    **compute**  $q^{j+1}$  via Equation (1) with Equation (7)  
    **compute**  $\psi^{j+1}$  via Equation (2) with Equation (9)  
    **update**  $\Sigma\psi$  and  $\Sigma q$  for  $R_f$   
**end for**  
**initialize**  $R_f$  from  $\psi^{1:N_{t_0}}$ ,  $\Sigma\psi$ ,  $q^{1:N_{t_0}}$ , and  $\Sigma q$   
**generate** true trajectories and observational data  
**for**  $j \leftarrow N_{t_0}$  **to**  $N_t$  **do**  
    **form**  $A_0, A_1, a_0, a_1$  using numerical discretization of Equations (21) and (22)  
    **compute** prior using Euler-Maruyama method for Equations (10) and (11)  
    **compute** posterior mean via Equation (12) and covariance via Equation (13)  
**end for**  
**return** posterior means and covariances and evaluate skill scores

---

**Remark 3.1**

We remark that the direct use of Equation (16) seems to be the most straightforward setting for writing the system into the CGNS framework. However, we found that this setting led to divergent results in our numerical experiments. This may be due to the strong decoupling between the layers, i.e.,  $\psi_1$  and  $\psi_2$ . Equation (16) shows that the left- and right-hand side terms are of different layers of information. Nonetheless, the effectiveness of the proposed method will be demonstrated in the numerical experiments presented in Section 4 below.

## 4 Numerical experiments

In this section, we study three numerical simulation scenarios for each initial streamfunction (sinusoidal and Gaussian in Table 2). Firstly, the CGNS framework that observes both layers of the QG model in Section 3.2 is simulated along with the numerical solution in Section 2 by following Algorithms 1 and 2, respectively. Similarly, the DA for recovering the second layer  $\psi_2$  given only the first layer  $\psi_1$  is simulated with Algorithm 3. Finally, we consider a simplified scenario where sea ice floe dynamics is coupled with the ocean flow modeled by the two-layer QG model. In all

these simulations, all the other settings such as the parameters for the temporal and spatial discretizations and DA noise strength, are given in Table 2 and Section 3. The processor that run the simulation is Intel i3-8130U CPU with 8GB RAM. This low computational demand is in line with recent QG DA study regarding efficient and low-cost implementations [31]. All the artifacts, including the MATLAB code, simulation videos, and performance evaluation, can be found in the [Github repository](#) [35].

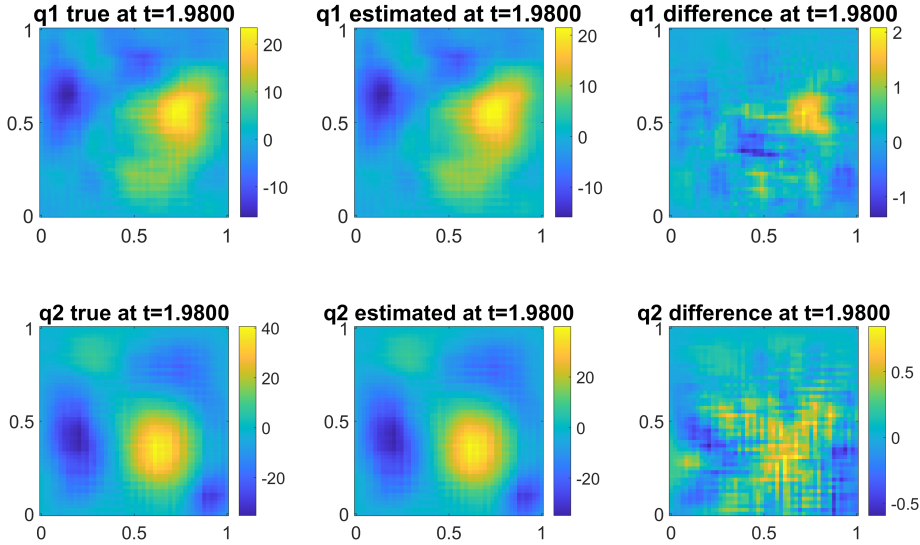


Figure 2: Simulation of true and recovered  $q$  at  $t = 1.98$  with sinusoidal streamfunction.

#### 4.1 EuDA for recovery of the vorticity and the second-layer flow

Figures 2 to 5 illustrate the DA simulations of Algorithms 2 and 3 compared with the results using Algorithm 1 on finer grid as true states, respectively. Qualitatively speaking, all DA estimated states visually seem to be indistinguishable from their true values across the two streamfunctions. Their errors (shown as Euclidean differences) are shown in the last columns of these Figures. Nevertheless, the explicit visualization of the difference (in relative scale of the original state) between the recovery and the truth reveals further insights for each recovery. For the recovery of the vorticity, the magnitude of the difference tends to follow that of the recovered attribute. For example, Figure 3 indicates the difference is most notable in the center, where the main flow is present. This trend does not hold for the recovery of the second-layer flow  $\psi_2$ . It can be seen that the difference for DA recovery of  $\psi_2$  mostly resembles noise. Overall, the errors remain small relative to the scale of the original states, resulting in low RMSEs, as demonstrated quantitatively below.

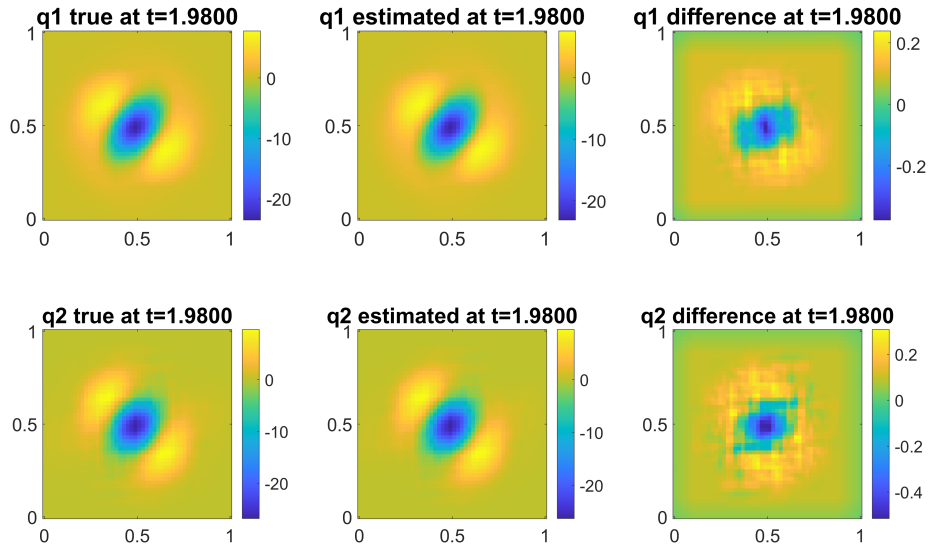


Figure 3: Simulation of true and recovered  $q$  at  $t = 1.98$  with Gaussian streamfunction.

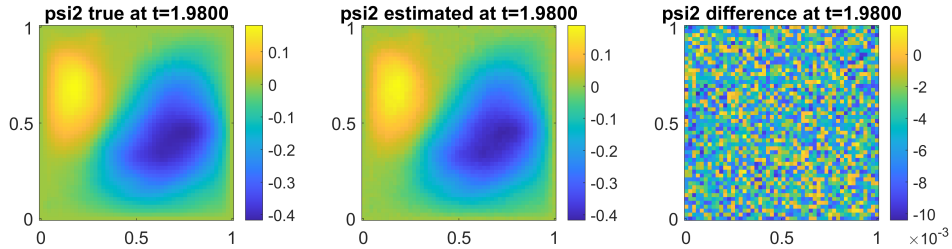


Figure 4: Simulation of true and recovered  $\psi_2$  at  $t = 1.98$  with sinusoidal streamfunction.

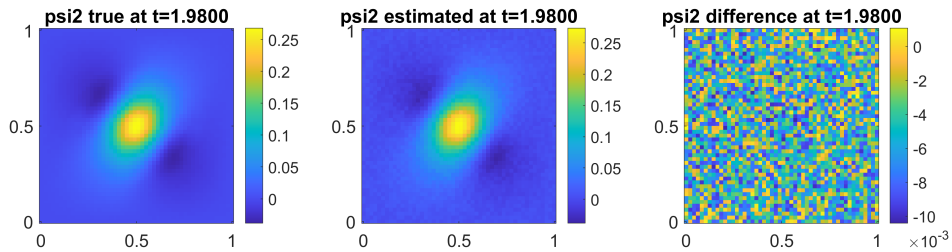


Figure 5: Simulation of true and recovered  $\psi_2$  at  $t = 1.98$  with Gaussian streamfunction.

To quantitatively evaluate the performance of the main algorithm (Algorithm 3), root mean squared error (RMSE) and pattern correlation (Corr) are used as two path-wise metrics [34] across different dimensions with the meshes  $N_x \times N_y = \{10 \times 10, 30 \times 30, 50 \times 50\}$  and timesteps  $N_t =$

{500, 1000, 3000, 5000, 10000, 15000, 20000}. Both metrics are the most common ways to compare the posterior mean and truth. RMSE indicates the average deviation between the estimated state and true state. Meanwhile, Corr highlights how well the spatial pattern of the simulation aligns with the reference model. They are defined as follows. Let  $\mu$  and  $x$  be vectors for the posterior mean and truth of a recovered variable of each cell, respectively, with  $n$  being the dimension of the state vectors. Then,

$$\mathbf{RMSE} = \left( \sqrt{\frac{\sum_{i=1}^n (\mu_i - x_i)^2}{n}} \right) / \mathbf{std}(x), \quad (23)$$

$$\mathbf{Corr} = \frac{\sum_{i=1}^n ((\mu_i - \mathbf{mean}(\mu))(x_i - \mathbf{mean}(x)))}{\sqrt{\sum_{i=1}^n (\mu_i - \mathbf{mean}(\mu))^2} \sqrt{\sum_{i=1}^n (x_i - \mathbf{mean}(x))^2}}. \quad (24)$$

The RMSE is always non-negative, with lower RMSE values indicating a more accurate posterior mean estimate. Since the RMSE in Equation (23) is normalized by the standard deviation of the true data, an RMSE above 1 implies that the error in the posterior mean estimate exceeds the mean variation in the true data [34]. Pattern correlation ranges from -1 to 1, where larger absolute values denote greater similarity between the two profiles [34]. Typically, a reliable estimate achieves a pattern correlation above 0.5.

Figure 6 illustrates the results of RMSE, Corr, and computation time for the recovery of  $\psi_2$  using Algorithm 3. Herein, the final time  $T_f = 2$  and the time step size is  $dt = T_f/N_t$ . The normalized computation time refers to actual computation time divided by  $N_t \times N_x^2$  to depict the time complexity of the algorithm, which is often hard to capture in the original time plot, especially with only three coordinates for each line. Therefore, the linearity in the normalized graph apart from  $N_t = 500$  indicates the time complexity of  $O(N_t \times N_x^2)$ , which follows from an  $N_x \times N_y$  (where  $N_x = N_y$ ) matrix performing operations iteratively over  $N_t$  times. This can be further corroborated by comparing the raw computation time across different  $N_t$  when  $N_x$  is fixed to 50. For example,  $N_t = 5000$  and  $N_t = 10000$  in such settings lasted about 400 and 800 seconds, respectively, which is proportional to the ratio between the  $N_t$ s. Similarly,  $N_t = 20000$  indeed ran for 1800 seconds, which is roughly quadruple and double of the other two settings, respectively. Furthermore, it can be seen that the most involved simulation approximately took 30 minutes under the below-average computational resources, suggesting a low demand for such operations.

Meanwhile, the RMSE metric, plotted on a logarithmic x-axis, effectively captures the algorithm's performance across timesteps  $N_t$  and grid sizes  $N_x$ . Notably, RMSE values decrease steadily as  $N_t$  increases, showing that the error between the posterior mean estimate and the true state reduces over time. This decline in RMSE appears to converge toward a value around the noise strength 0.1, irrespective of the grid size. This convergence suggests that the DA algorithm achieves a consistent level of accuracy over time, largely independent of spatial resolution. In other words, as the time marching scheme progresses, the DA framework consistently refines its estimates, reinforcing

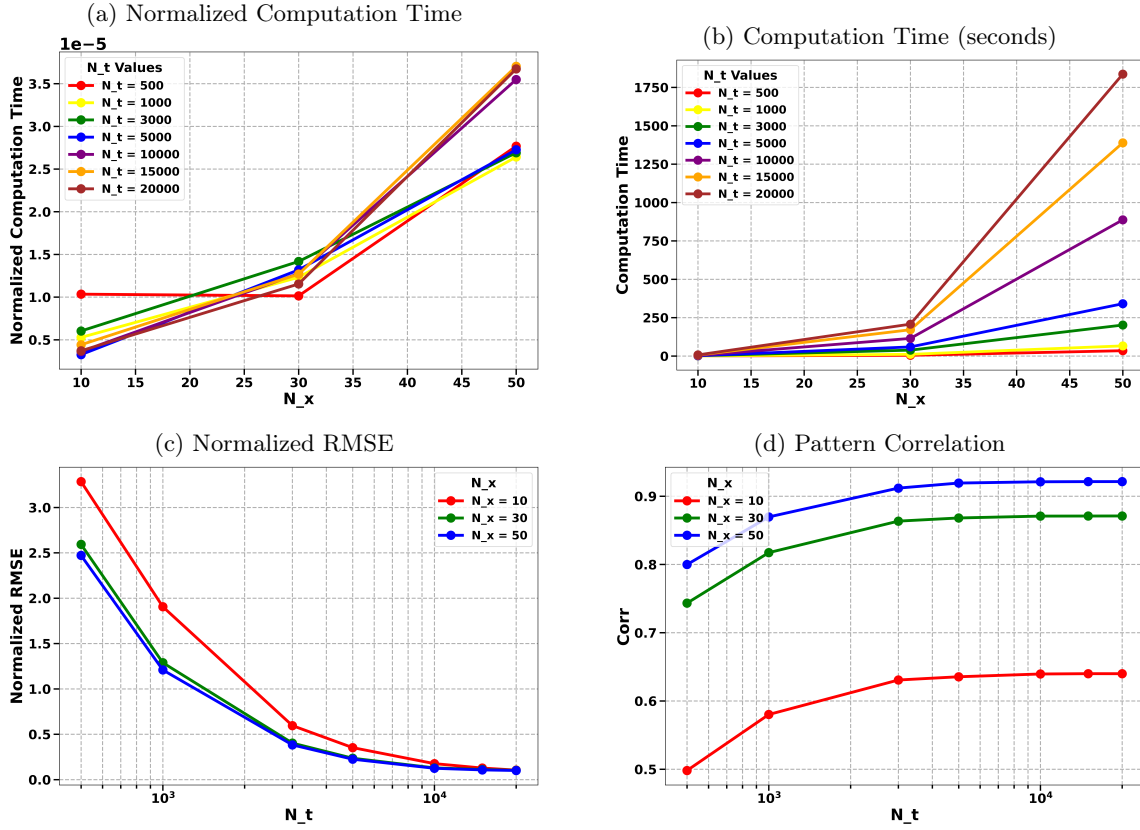


Figure 6: Performance evaluation of two-layer QG model simulation via CGNS.

its robustness across varying spatial scales. This outcome highlights one of DA’s primary strengths: its robustness and effectiveness in multiscale settings, where it can achieve reliable accuracy regardless of spatial granularity.

The Corr metric exhibits a general upward trend with respect to the number of timesteps across different grid sizes, indicating improved alignment between the model estimate and the true state as the assimilation process advances. However, the influence of  $N_x$  on Corr is significant. Larger grid sizes consistently yield higher Corr values, showing that higher spatial resolution enables the algorithm to better capture the pattern of the true state. For example, Corr is maximized at 0.92 for  $N_x = 50$ , while  $N_x = 10$  can go as high as 0.64. Interestingly, Corr values show diminishing returns after  $N_t = 3000$ , where further increases in  $N_t$  contribute less to improving Corr across all  $N_x$ . This observation suggests that while finer temporal resolution continues to provide marginal benefits, the spatial resolution ultimately becomes a limiting factor in the Corr metric’s growth. On the other hand, the model error and observation noise characterized by  $B_1$  and  $b_1$  in the DA

setting are also limiting factors for further improvement of the skill scores. This outcome implies the necessity of sufficiently high grid resolution  $N_x$  for more accurate state estimation when model error and observation noise are small. In summary, these numerical experiments indicate that EuDA of the two-layer QG model via CGNS performs well with decreasing RMSE and increasing Corr when refining the grids.

## 4.2 An application to sea ice floe dynamics with QG ocean flow

We now turn to an application of the EuDA framework to the two-layer QG model in the physical domain, with a focus on ocean-ice-floe dynamics. This study aims to demonstrate that the EuDA approach, when implemented directly in the physical domain under an Eulerian frame of reference, can be seamlessly coupled with the floe dynamics described in a Lagrangian frame, thereby providing a promising alternative framework for assimilating geophysical data. To emphasize the fundamental coupling mechanisms without introducing excessive complexity, we consider an idealized configuration that neglects floe–floe collisions and adopts a linear drag law to describe the ocean–ice interaction. This simplified configuration enables a pathway for coupling the EuDA-estimated states with floe dynamics described in the Lagrangian frame, capturing the essential dynamical feedback between the ocean circulation and the drifting sea ice. With this in mind, we consider the following governing model:

$$\frac{d\mathbf{x}_l}{dt} = \mathbf{v}_l, \quad (25)$$

$$\frac{d\mathbf{v}_l}{dt} = \beta(\mathbf{u} - \mathbf{v}_l), \quad (26)$$

$$\mathbf{u}_i = \left( -\frac{d\psi_i}{dy}, \frac{d\psi_i}{dx} \right), \quad (27)$$

where  $\psi_i, i = 1, 2$ , are the EuDA-estimated (using Algorithm 3) streamfunctions that produce the ocean velocities of the two layers.  $\beta$  is the ocean drag coefficient and  $\beta = 0.5$  is chosen in our simulations below.

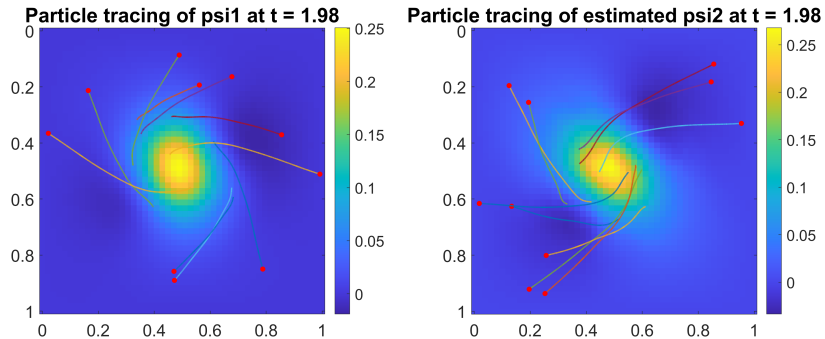


Figure 7: Simulation of particle tracing of two-layer QG model at  $t = 1.98$  with Gaussian streamfunction.

We first note that the streamfunctions are defined at the finite-difference nodal points of the Eulerian grid, while the floes evolve along Lagrangian trajectories. To reconcile this difference in reference frames, we perform a linear interpolation of the nodal values to reconstruct the streamfunctions over the entire physical domain. The interpolated values are then evaluated at each floe position  $\mathbf{x}_l$  to compute the ocean drag force via Equation (26). With this postprocessed Eulerian state, we assume that each floe is subject to drag forces from one of the ocean layers. The resulting trajectories, illustrated in Figure 7, reveal the influence of the two-layer flow fields on floe motion and highlight the potential of using Lagrangian floe observations to infer the underlying ocean velocities in the physical domain. This observation further suggests that Lagrangian and Eulerian observational data can be jointly assimilated within a unified multiscale framework to enhance filtering in highly complex, coupled ice–ocean systems (thus, generalizing [12] to ocean flow in the physical domain). This is subject to future work.

## 5 Conclusion

This study developed an EuDA framework by integrating CGNS for a two-layer QG model in the physical domain. The results demonstrate that this framework maintains low RMSE values across time and grid resolutions while achieving strong spatial alignment with the true state. The pattern correlation analysis highlights the framework’s capacity to adapt across multiple scales, revealing that further improvements can be made when using a finer grid. These findings collectively affirm the robustness and scalability of the proposed EuDA formulation, providing a foundation for more advanced data assimilation strategies in physical domains.

Building on these outcomes, several promising directions for future work are as follows. Firstly, one may leverage neural networks (NN) on a cell-by-cell basis, which represents a key pathway toward parallelizing the computational processes inherent in the proposed framework. This ap-

proach could allow efficient parallelization that maximizes computational efficiency [26]. Another intriguing extension involves exploring whether the fundamental state variables can be accurately recovered solely by coupling the QG model with sea ice particle dynamics, with observation of the particle displacements. Current methods primarily rely on direct observations of  $\psi$  and  $q$ , but a system where only particle trajectories are observed could offer a more feasible setup in real-world applications. This approach would require developing advanced techniques, such as the recently developed Lagrangian-Eulerian multiscale DA (LEMDA) [12], to reconstruct field states from sparse data in the physical domain.

Furthermore, it is essential to establish rigorous analytical conditions for the convergence of the two-layer QG CGNS solver, ensuring stability across various parameter settings. Such conditions would enable precise control over model parameters and provide clear boundaries within which the solver maintains both accuracy and stability. It would serve as a critical tool for designing and fine-tuning the DA process, allowing researchers to optimize computational resources without compromising the fidelity of the posterior mean estimate [21]. Extending the two-layer QG model to support more layers would offer the potential for modeling complex systems that may involve more extreme vertical stratification, such as those found in oceanographic and atmospheric flows [27, 7]. Each additional layer would introduce unique challenges related to inter-layer coupling and the propagation of uncertainties through the model, thus requiring a refined DA framework. In this respect, the proposed two-layer framework can serve as an inductive step for a scalable approach, incrementally increasing model complexity.

In conclusion, this work has laid a foundation for advancing data assimilation in the physical domain by demonstrating a EuDA framework based on CGNS. The proposed approach provides a coherent and computationally efficient alternative for assimilating nonlinear, high-dimensional systems, paving the way for more accurate and interpretable physical-domain modeling.

## Acknowledgments

Q.D. is partially supported by start-up funding from the Yau Mathematical Sciences Center, Tsinghua University, the Australian National Computing Infrastructure (NCI) national facility under grant zv32, and the HMI Computing for Social Good Seed Research Grant.

## References

- [1] Peter Bauer, Alan Thorpe, and Gilbert Brunet. The quiet revolution of numerical weather prediction. *Nature*, 525(7567):47–55, 2015.
- [2] Jule G. Charney. The Dynamics of Long Waves in a Baroclinic Westerly Current. *Journal of Meteorology*, 4(5):136–162, 1947.

- [3] Jean-Paul Chehab and Maithem Trabelsi Moalla. Numerical simulations of a 2D quasi geostrophic equation, 2010.
- [4] Nan Chen. *Stochastic Methods for Modeling and Predicting Complex Dynamical Systems*. Springer, 2023.
- [5] Nan Chen, Yingda Li, and Honghu Liu. Conditional Gaussian Nonlinear System: A Fast Preconditioner and a Cheap Surrogate Model for Complex Nonlinear Systems. *Chaos: An Interdisciplinary Journal of Nonlinear Science*, 32(5):053122, May 2022. Part of the Focus Issue on Theory-informed and Data-driven Approaches to Advance Climate Sciences.
- [6] Nan Chen and Andrew J Majda. Conditional Gaussian systems for multiscale nonlinear stochastic systems: Prediction, state estimation and uncertainty quantification. *Entropy*, 20(7):509, 2018.
- [7] Colin Cotter, Dan Crisan, Darryl Holm, Wei Pan, and Igor Shevchenko. Data Assimilation for a Quasi-Geostrophic Model with Circulation-Preserving Stochastic Transport Noise. *Journal of Statistical Physics*, 179(5):1186–1221, 2020.
- [8] J Austin Cottrell, Thomas JR Hughes, and Yuri Bazilevs. *Isogeometric analysis: toward integration of CAD and FEA*. John Wiley & Sons, 2009.
- [9] Richard Courant, Kurt Friedrichs, and Hans Lewy. Über die partiellen Differenzengleichungen der mathematischen Physik. *Mathematische Annalen*, 100(1):32–74, 1928.
- [10] H.C. Davies and H. Wernli. Quasi-geostrophic theory. In James R. Holton, editor, *Encyclopedia of Atmospheric Sciences*, pages 1787–1794. Academic Press, Oxford, 2003.
- [11] Quanling Deng, Pouria Behnoudfar, and Victor M Calo. SoftIGA: Soft isogeometric analysis. *Computer Methods in Applied Mechanics and Engineering*, 403:115705, 2023.
- [12] Quanling Deng, Nan Chen, Samuel Stechmann, and Jiuhua Hu. LEMDA: A Lagrangian-Eulerian Multiscale Data Assimilation Framework, 2024.
- [13] Quanling Deng and Alexandre Ern. SoftFEM: revisiting the spectral finite element approximation of second-order elliptic operators. *Computers & Mathematics with Applications*, 101:119–133, 2021.
- [14] Alexandre Ern and Jean-Luc Guermond. *Theory and practice of finite elements*, volume 159. Springer, 2004.
- [15] Geir Evensen. Sequential data assimilation with a nonlinear quasi-geostrophic model using Monte Carlo methods to forecast error statistics. *Journal of Geophysical Research: Oceans*, 99(C5):10143–10162, 1994.
- [16] Geir Evensen. *Data Assimilation: The Ensemble Kalman Filter*. Springer Science & Business Media, 2009.
- [17] Heiner Kornich, S Wahl, and S Basu. Dynamic downscaling of atmospheric fields for mesoscales and sub-mesoscales. *Journal of Geophysical Research: Atmospheres*, 113:D07108, 2008.
- [18] Nathan Kutz. *Data-Driven Modeling & Scientific Computation*. Oxford University Press, 2013.
- [19] Kody Law, Andrew Stuart, and Konstantinos Zygalakis. *Data Assimilation: A Mathematical Introduction*. Springer, 2015.

- [20] Robert S Liptser and Albert N Shiryaev. *Statistics of random processes II: Applications*, volume 6. Springer Science & Business Media, 2013.
- [21] Andrew J Majda and John Harlim. A new perspective on multiscale geophysical data assimilation. *SIAM Review*, 54(2):377–418, 2012.
- [22] Andrew J. Majda, John Harlim, and Boris Gershgorin. Mathematical strategies for filtering turbulent dynamical systems. *Discrete and Continuous Dynamical Systems - Series A*, 27(2):441–486, 2010.
- [23] HT. Tachim Medjo. Numerical Simulations of a Two-Layer Quasi-Geostrophic Equation of the Ocean. In *SIAM Journal on Numerical Analysis*, 2000, vol 37, pages 2005–2022. Society for Industrial and Applied Mathematics, 2000.
- [24] Eiichi Oka. *Nonlinear Solutions to a Two-Layer Quasi-Geostrophic Model of the Gulf Stream*. PhD thesis, Old Dominion University, Shimizu, Japan, December 1989.
- [25] Bernt Oksendal. *Stochastic Differential Equations: An Introduction with Applications*. Springer, 6 edition, 2010.
- [26] Jaideep Pathak, Zhixin Lu, Brian Hunt, Michelle Girvan, and Edward Ott. Using machine learning to augment coarse-grid computational fluid dynamics simulations. *Journal of Computational Physics*, 375:973–991, 2018.
- [27] Joseph Pedlosky. *Geophysical Fluid Dynamics*. Springer Science & Business Media, 1987.
- [28] S. G. Penny, E. Bach, K. Bhargava, C.-C. Chang, C. Da, L. Sun, and T. Yoshida. Strongly Coupled Data Assimilation in Multiscale Media: Experiments Using a Quasi-Geostrophic Coupled Model. *Journal of Advances in Modeling Earth Systems*, 11(6):1803–1829, 2019.
- [29] Di Qi and Andrew J Majda. Low-dimensional reduced-order models for statistical response and uncertainty quantification: Two-layer baroclinic turbulence. *Journal of the Atmospheric Sciences*, 73(12):4609–4639, 2016.
- [30] Michael Roth, Gustaf Hendeby, Carsten Fritsche, and Fredrik Gustafsson. The Ensemble Kalman filter: a signal processing perspective. *EURASIP Journal on Advances in Signal Processing*, 2017.
- [31] François Rozet and Gilles Louppe. Score-based Data Assimilation for a Two-Layer Quasi-Geostrophic Model, 2023.
- [32] Geoffrey K. Vallis. *Atmospheric and Oceanic Fluid Dynamics*. Second Edition. Cambridge University Press, 2017.
- [33] Zhongrui Wang, Nan Chen, and Di Qi. A Nonlinear Data Assimilation Algorithm with Closed-Form Approximations for Multi-Layer Flow Fields. *Monthly Weather Review*, 2025.
- [34] Daniel S. Wilks. *Statistical Methods in the Atmospheric Sciences*. Academic Press, 3rd edition, 2011.
- [35] Geun Yun. Quasi\_geostrophic\_model\_for\_lemda. [https://github.com/geun-yun/Quasi\\_geostrophic\\_model\\_for\\_LEMDA/tree/main](https://github.com/geun-yun/Quasi_geostrophic_model_for_LEMDA/tree/main), 2024.